On Deflections of Vertical Determined From HY-2A/GM Altimetry Data in the Bay of Bengal

Hui Ji, Jinyun Guo, Chengcheng Zhu, Jiajia Yuan, Xin Liu, and Guowei Li

***Abstract*—Satellite altimetry is an important technique to derive oceanic deflections of vertical (DOV). HaiYang-2A (HY-2A) is the first Chinese altimetry satellite launched in August 2011 to observe the global marine dynamic environment. To assess the reliability of DOVs derived from HY-2A geodetic mission data, the Bay of Bengal and its adjoining area (0°–23°N, 80°–100°E) are selected as the research area, and the accuracy of HY-2A/GM-derived DOVs is compared with that of DOVs determined from CryoSat-2-measured sea surface heights (SSHs) and SARAL/AltiKa (SARAL)-measured SSHs which are in the same period as HY-2A-measured SSHs. Compared with the along-track DOVs calculated from Sentinel-3B-measured SSHs (from cycle 20 to cycle 33), the RMS of differences for HY-2A-determined DOVs is 0.1 μrad smaller than that for SARAL-determined DOVs and CryoSat-2-determined DOVs. The differences of the along-track DOVs in the frequency domain are also analyzed by power spectral density. In addition, the XGM2019e model is adopted to evaluate the quality of the gridded DOVs model established by least-squares collocation method. Marine gravity anomaly models (SIO V30.1) and ship-borne gravity anomalies are also used to assess the accuracy of gravity anomalies derived from gridded DOVs. The whole results show that the accuracy of HY-2A-determined DOVs is coincident with that of CryoSat-2-determined DOVs and slightly lower than that of SARAL-determined DOVs. Therefore, HY-2A/GM altimetry data can be applied in establishing the global high-precision DOV model.**

***Index Terms*—Bay of Bengal (BOB), cryosat-2, HY-2A/GM, least-squares collocation, oceanic deflection of vertical (DOV), SARAL/AltiKa, satellite altimetry.**

I. Introduction

In THE past decades, satellite altimetry as a space technology has played an important role in the development of marine geodesy [1]–[3], geophysics [4], [5], and oceanography [6]–[8]. Satellite altimeter directly observes the range between satellite and nadir sea surface, significant wave height and backscattering coefficient by transmitting and receiving radar pulse signals. Compared with traditional marine surveying, such as tide gauge, measuring ship and buoy, the sea surface observations collected by satellite altimeter have the advantages of wide range, high accuracy, large amount of data and high repeatability. Therefore, altimetry data have gradually become an important data source for the study of ocean geoid, oceanic deflections of vertical (DOVs), marine gravity anomalies, ocean surface wind field, ocean tide, mesoscale eddies and ocean circulation [9]–[11].

DOVs [12]–[14] are important data for establishment of geoid model and earth gravity field model, and study on the change of earth mass. The traditional techniques for DOV determination include astrogeodesy, astrogravimetry, gravimetry, and GNSS leveling. Due to the existence of disturbance factors such as sea surface wave, ocean current and ocean tide, it is difficult to determine the marine DOVs by traditional techniques, so calculating high-precision and high-resolution marine DOVs have attracted wide attention. With the development of satellite altimetry, the recovery of oceanic DOVs from altimeter data is studied. The $1' \times 1'$ oceanic DOV model was established from multi-satellite altimetry data and gravity anomaly data [15], and a new approximate relationship between DOVs and gravity anomalies was proposed [16]. At present, there are three main approaches to calculate the oceanic DOVs from altimeter data, which are proposed by Sandwell [17], Olgiati *et al.* [18] and Hwang *et al.* [19], respectively. The process of obtaining DOVs can eliminate the influence of long-wavelength error and DOV can be used to inverse gravity anomaly.

More and more ocean satellites are successfully launched. HY-2A [20], [21] is the first marine dynamic environment satellite developed by China. It was launched in August 2011. In March 2016, it changed its orbit to carry out geodetic mission (GM) with a repeat period of 168 days, and stopped collecting data in September 2020. The objective of HY-2A mission is to use microwave sensors to detect the ocean dynamic environment, sea surface wind field, sea surface height and sea surface temperature. Since the successful launch of HY-2A, the accuracy of HY-2A altimeter data is discussed. The quality and system performance of HY-2A altimeter data are evaluated [22], [23], and the accuracy of gravity anomalies derived from HY-2A/GM altimetry data in the South China Sea is assessed [24].

This article aims to assess the accuracy of HY-2A/GM altimeter data in estimating DOVs over the Bay of Bengal (BOB). The accuracy of DOVs derived from HY-2A/GM altimeter data is compared with that of DOVs derived from SARAL/AltiKa (SARAL) and CryoSat-2 altimeter data. In Section II, the research area and data are introduced. Altimeter data of

Manuscript received June 23, 2021; revised October 17, 2021; accepted November 16, 2021. Date of publication November 19, 2021; date of current version December 6, 2021. This work was supported in part by the National Natural Science Foundation of China under Grant 41774001, in part by the Autonomous and Controllable Special Project for Surveying and Mapping of China under Grant 816-517, and in part by SDUST Research Fund under Grant 2014TDJH101. *(Corresponding author: Jinyun Guo.)*

Hui Ji, Jinyun Guo, Chengcheng Zhu, Jiajia Yuan, and Xin Liu are with the College of Geodesy and Geomatics, Shandong University of Science and Technology, Qingdao 266590, China (e-mail: jihui@sdust.edu.cn; jinyunguo1@126.com; zhucheng963@126.com; yuanjiajia2008@126.com; xinliu1969@126.com).

Guowei Li is with the Shandong Provincial Institute of Land Surveying and Mapping, Jinan 250102, China (e-mail: liguowei_2021@126.com).

Digital Object Identifier 10.1109/JSTARS.2021.3129273

TABLE I
INFORMATION OF THREE SATELLITE ALTIMETRY DATA

Satellite mission	band	Repeat period/d	Inter-track distance at equator /km	Latitude range/°	Data amount (SSH)	Time span
HY-2A/GM	Ku/C	168	15	±81	521809	16.07-20.06 (cycle129-288)
SARAL-DP	Ka	-	-	±81.5	534457	16.07-20.06 (cycle100-140)
CryoSat-2 LRM	Ku/C	369	7.5	±88	641238	16.06-20.06 (cycle82-131)

HY-2A/GM, SARAL-drifting phase (SARAL-DP) and CryoSat-2 in the same period are selected. Section III presents in detail the method for calculating the meridional component and the prime vertical component of DOVs from altimeter-measured sea surface heights (SSHs), and the method for deriving gravity anomalies from DOVs is also described. In Section IV-B, the along-track DOVs at observation points of Sentinel-3B are used to assess the accuracy of gridded DOVs determined from altimeter data, and their differences in the wave number domain are discussed. Then, the XGM2019e-DOV model is also used to evaluate the accuracy of the meridional component and the prime vertical component of altimeter-determined DOVs. In Section IV-C, the gravity anomaly model derived from the gridded DOVs is established, and the accuracy of gravity anomaly derivation is evaluated by using National Centers for Environmental Information (NCEI) ship-borne gravity anomalies and SIO V30.1-GRA model. Section V gives the conclusion.

II. RESEARCH AREA AND DATA

A. Research Area

The BOB and its adjoining areas (0°–23°N, 80°–100°E) are selected as the research area. The research area contains many special terrains such as basins and islands. In addition, as the largest turbidite alluvial fan in the world, the BOB collects plenty of terrigenous matter from the Qinghai-Tibet Plateau and the Indian peninsula, and is an ideal area for the study of land and ocean interaction [25], [26].

B. Altimetry Data

In order to assess the reliability of HY-2A/GM altimetry data in calculating DOVs, the accuracy of SARAL/AltiKa (SARAL) and CryoSat-2 altimetry data in calculating DOVs is compared with that of HY-2A/GM-derived DOVs. The altimetry data of the three satellites are all from the global 1 Hz along-track Level-2 + (L2P) version 2.0 SLA product (including sea level anomaly and its components, and validity flags). Table I gives the information of the selected three satellites. L2P product is the result of reprocessing geophysical data record, that provided by archiving, validation, and interpretation of satellite oceanographic.[1] The reprocessing includes updating corrections and a quality control on altimeter data [27]. The reference ellipsoid used for L2P version 2.0 SLA product (including HY-2A, SARAL and CryoSat-2) is the TOPEX/Poseidon ellipsoid.

HY-2A [28] was successfully launched from Taiyuan Space Center in August 2011. It is the first marine dynamic environment satellite successfully planned by China to perform altimetry and scattering measurement missions. HY-2A carried out 14-day exact repeat mission at the altitude of 971 km and 168-day repeated GMs at the altitude of 973 km. The orbit of HY-2A is sun-synchronous with an inclination of 99.3°. HY-2A is mainly equipped with microwave sensor, dual-frequency radar altimeter and Ku-band scatterometer.

SARAL [29], [30] is a satellite jointly developed by Indian Space Research Organisation and Centre National d'Etudes Spatiales (CNES), which was successfully launched in February, 2013. AltiKa altimeter uses Ka-band (35 GHz) for the first time, and its working frequency is higher than all previous radar altimeters. Therefore, AltiKa altimeter can obtain better observations in coastal and land areas. After July 2016, the SARAL ground track drifted and the repeated ground track could not be maintained, so the new phase is named "SARAL-DP."

CryoSat-2 [31]–[33], developed by European Space Agency for polar observation, was successfully launched in April 2010. The altimeter (synthetic aperture interferometric altimeter, SIRAL) on CryoSat-2 innovatively have three working modes: low resolution mode (LRM); synthetic aperture radar mode (SAR); and synthetic aperture radar interferometry mode. The L2P product data of CryoSat-2 mission are mainly collected in LRM.

It can be seen from the ground tracks of the three satellites (see Fig. 1) that CryoSat-2 has the highest spatial resolution and the densest tracks, because it has a 369-day repeat period. The nominal inter-track distance of CryoSat-2 is 7.5 km, and the ground track is allowed to drift within 5 km [34]. In addition, the ground tracks of HY-2A have high reproducibility.

C. Data for Assessment

In this article, altimetry data of Sentinel-3B [35] from cycle 20 to cycle 33 of L2P product are used to assess the along-track DOVs calculated from altimetry data of three satellites. Sentinel-3B was successfully launched in April 2018 with an altitude of 815 km and orbital inclination of 98.6°, the cycle duration was 27 days. The main purpose of Sentinel-3B surface topography mission which works at Ku band is to measure sea surface topography, SSHs and significant wave height with high accuracy and reliability.

[1] [Online]. Available: https://www.aviso.altimetry.fr/

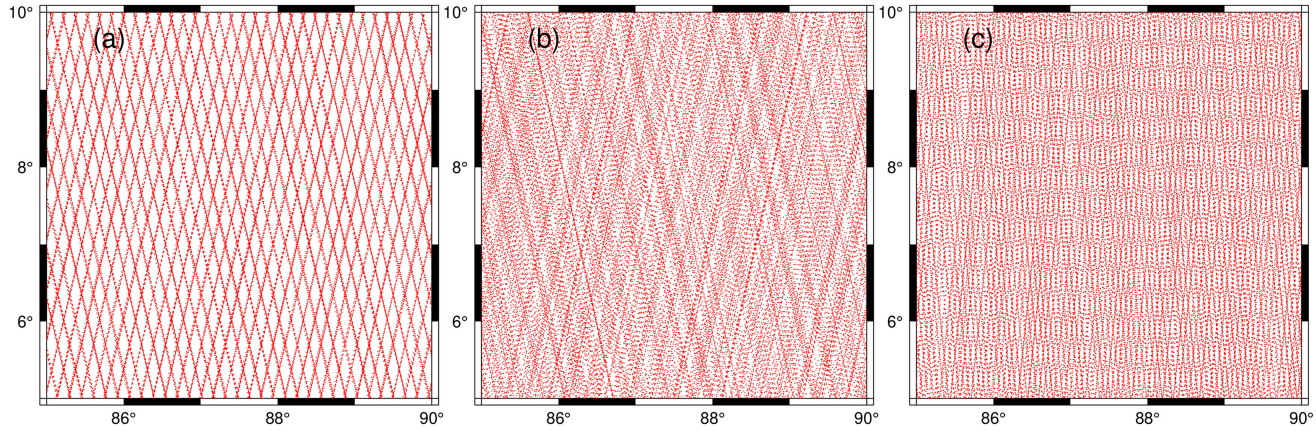

Fig. 1. Ground tracks of three satellites. (a) Distribution of HY-2A's ground tracks (cycle129-288). (b) Distribution of SARAL's ground tracks (cycle100-140). (c) Distribution of CryoSat-2's ground tracks (cycle82-131).

SIO V30.1-DOV and SIO V30.1-GRA [36] are respectively high-resolution and high-precision DOV model and marine gravity field model with $1'\times1'$ resolution published by the scripps institution of oceanography (SIO) of the University of California, San Diego. The main improvement of SIO V30.1 with respect to SIO V29.1 is to add the latest altimetry data of SARAL, CryoSat-2 and Sentinel-3A/B. In addition, the filtering wavelength in shallow water is changed to 14 km. It is worth noting that HY-2A altimetry data were not used in the construction of SIO V30.1 model.

XGM2019e [37] is a spherical harmonic model of the Earth's gravitational potential constructed by combination of three major data sources: longer wavelength ranging up to d/o 300 provided by the combined satellite model GOCO06s, the $15'$ augmented with topography induced gravity anomalies over land provided by the NGA and the $1'\times1'$ marine gravity anomalies provided by DTU2013. XGM2019e is represented by a spherical harmonic function, and its degree and order (d/o) reach 5399. The XGM2019e-DOV and XGM2019e-GRA used for accuracy evaluation is the DOV model and gravity anomaly model obtained from XGM2019e_2159 (d/o are 2159[2]).

In order to test the accuracy of gravity anomalies derived from DOVs, the ship-borne free air gravity anomalies provided by the NCEI [38]–[40] is adopted. Ship-borne gravimetry is less affected by time-varying sea surface topography, and has high accuracy in nearshore area. There are 27 routes in the study area, and the measuring time is from 1963 to 2008. The distribution of ship-borne gravity anomalies over the BOB is shown in Fig. 2.

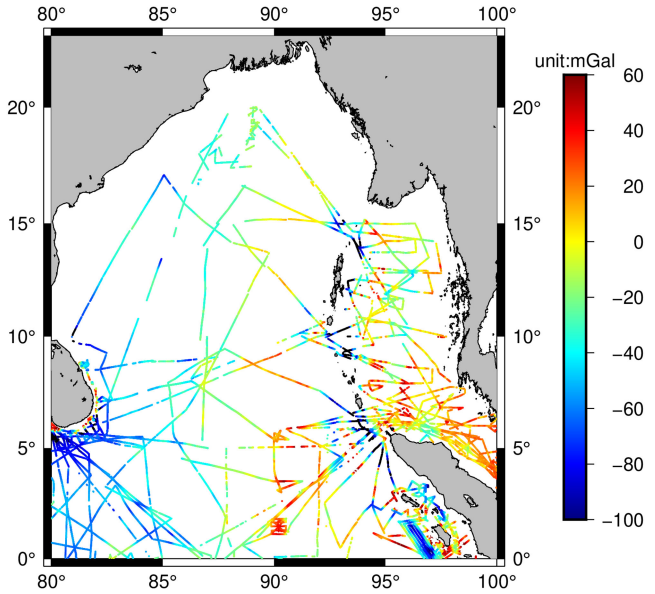

Fig. 2. Distribution of free air gravity anomalies in the BOB.

III. Methods

A. Gridded DOVs' Derivation

DOVs are calculated by the least-squares collocation (LSC) method [41]–[43]. The LSC combines calculation of DOVs and grid transformation of DOVs into one step.

First, the influence of sea surface topography (CNES-CLS18 MDT) [44] is removed from the preprocessed SSHs (after instrument error correction, propagation error correction and geophysical correction) to obtained the geoid height N. Then, according to the difference of geoid height ∂N at two adjacent along-track observation points, the along-track geoid gradient is obtained as $\frac{\partial N}{\psi}$, where ψ is the spherical distance between the two points. Then, the remove-restore method is used to remove the along-track geoid gradient calculated by the reference gravity field model (EGM2008, [45]) from the altimeter-determined along-track geoid gradient, and the residual along-track geoid gradients and the residual along-track DOVs ε ($\varepsilon = -\frac{\partial N}{\psi}$) are obtained (the along-track geoid gradient and the along-track DOV are equal and their directions are opposite).

Then, the meridian component ξ and the prime vertical component η of residual gridded DOVs [4], [46] [47] are computed

[2][Online]. Available: http://icgem.gfz-potsdam.de/calcgrid

by LSC

$$\begin{pmatrix} \xi \\ \eta \end{pmatrix} = \begin{pmatrix} C_{\xi\varepsilon} \\ C_{\eta\varepsilon} \end{pmatrix} (C_{\varepsilon\varepsilon} + C_{nn})^{-1}\varepsilon \tag{1}$$

where $C_{\xi\varepsilon}$ is the covariance matrix for the meridian component of gridded DOVs and the along-track DOVs, $C_{\eta\varepsilon}$ is the covariance matrix for the prime vertical component of gridded DOVs and the along-track DOVs, $C_{\varepsilon\varepsilon}$ is the variance matrix for the along-track DOVs, C_{nn} is the noise variance matrix for the along-track DOVs, and ε is the matrix for the along-track DOVs.

The variance functions of two deflection components (ξ, η) are not isotropic. However, the variance functions of the longitudinal component (l) and the transverse component (m) of DOV are isotropic. Then for theoretical discussions it is more convenient to calculate $C_{\xi\varepsilon}$, $C_{\eta\varepsilon}$ and $C_{\varepsilon\varepsilon}$ by the variance functions of the longitudinal and the transverse component.

The meridian and prime vertical components of residual gridded DOV (ξ_p, η_p) at point P are expressed by the longitudinal and the transverse components (l_p, m_p) of the DOV as

$$\begin{aligned} \xi_p &= l_p \cos\alpha_{pq} - m_p \sin\sin\alpha_{pq} \\ \eta_p &= l_p \sin\alpha_{pq} + m_p \sin\cos\alpha_{pq}. \end{aligned} \tag{2}$$

The residual along-track DOV at point p and q $(\varepsilon_p, \varepsilon_q)$ [48] are expressed by the longitudinal and the transverse components of the DOV as

$$\begin{aligned} \varepsilon_p &= -l_p \cos(\alpha_{\varepsilon_p} - \alpha_{pq}) - m_p \sin(\alpha_{\varepsilon_p} - \alpha_{pq}) \\ &= l_p \cos(\alpha_{\varepsilon_p} - \alpha_{qp}) + m_p \sin(\alpha_{\varepsilon_p} - \alpha_{qp}) \\ \varepsilon_q &= l_q \cos(\alpha_{\varepsilon_q} - \alpha_{qp}) + m_q \sin(\alpha_{\varepsilon_q} - \alpha_{qp}) \end{aligned} \tag{3}$$

where α_{ε_p} and α_{ε_q} represent the azimuth of the along-track DOV at subsatellite point P and Q, respectively; α_{pq} and α_{qp} represent the azimuth from p to q and the azimuth from q to p, respectively.

Therefore, the covariance between the two deflection components of the residual gridded DOV and the residual along-track DOV ($C_{\xi\varepsilon}$, $C_{\eta\varepsilon}$), and the variance of the residual along-track DOV ($C_{\varepsilon\varepsilon}$) [49] can be expressed as

$$\begin{aligned} C_{\xi\varepsilon} &= C_{ll} \cos\alpha_{pq} \cos(\alpha_{\varepsilon_q} - \alpha_{qp}) \\ &\quad - C_{mm} \sin\alpha_{pq} \sin(\alpha_{\varepsilon_q} - \alpha_{qp}) \\ C_{\eta\varepsilon} &= C_{ll} \cos\alpha_{pq} \cos(\alpha_{\varepsilon_q} - \alpha_{qp}) \\ &\quad + C_{mm} \sin\alpha_{pq} \sin(\alpha_{\varepsilon_q} - \alpha_{qp}) \\ C_{\varepsilon\varepsilon} &= C_{ll} \cos(\alpha_{\varepsilon p} - \alpha_{qp}) \cos(\alpha_{\varepsilon_q} - \alpha_{qp}) \\ &\quad + C_{mm} \sin(\alpha_{\varepsilon p} - \alpha_{qp}) \sin(\alpha_{\varepsilon_q} - \alpha_{qp}) \end{aligned} \tag{4}$$

where, C_{ll} and C_{mm} are determined by the covariance function of the Earth's disturbing potential $K(\psi)$ in Moritz [50].

Finally, the accuracy of the along-track DOVs needs to be obtained. The discrepancy of SSHs after crossover adjustment can be adopted to evaluate the accuracy of the along-track DOVs determined by Ku-band altimeters. Therefore, the noise variance of the along-track DOVs C_{nn} can be calculated by

$$C_{nn} = (m_\varepsilon)^2 = \left(\frac{\sqrt{2} m_{SSH}}{\overline{\psi}}\right)^2 = \left(\frac{m_\Delta}{\overline{\psi}}\right)^2 \tag{5}$$

where m_ε is the STD of the along-track DOVs determined by Ku-band altimeters, m_{SSH} is the STD of SSHs, m_Δ is the STD of discrepancy of SSHs at crossover points, and $\overline{\psi}$ is the average spherical distance of two adjacent points.

The frequency of Ka-band altimeter is higher than that of Ku-band altimeter, so the penetration ability of Ka-band signal is weaker than Ku-band signal, which leads to the greater influence of tropospheric refraction error on Ka-band SSHs. In addition, the crossover adjustment cannot correct the propagation error caused by cloud and rain weather. Therefore, the accuracy of the along-track DOVs determined by Ka-band altimeter is not suitable to be evaluated by the discrepancy of SSHs at crossover points, and should be calculated by another method.

The gravity anomaly derived by LSC is based on along-track DOVs. When LSC is used to derived the gravity anomalies, the STD of the derived gravity anomaly is calculated as follows:

$$C_{\Delta\widehat{g}} = (m_{\Delta\widehat{g}})^2 = C_{\Delta g\Delta g} - C_{\Delta g\varepsilon}(C_{\varepsilon\varepsilon} + C_{nn})^{-1} C_{\varepsilon\Delta g} \tag{6}$$

in which $C_{\Delta\hat{g}}$ is the variance matrix for gravity anomalies estimation, $C_{\Delta g\Delta g}$ and $C_{\varepsilon\varepsilon}$ are the variance matrix for gravity anomalies and DOVs, respectively, $C_{\varepsilon\Delta g}$ is the covariance matrix for DOVs and gravity anomalies, and C_{nn} is the noise variance for DOVs. $m_{\Delta\hat{g}}$ is the STD of altimeter-derived gravity anomalies.

As the accuracy of gravity anomalies increases with the accuracy and density of the along-track DOVs, (6) can be simplified into an empirical formula between the precision of gravity anomalies, the precision of the along-track DOVs m_ε and the density of the along-track DOVs (the average of the along-track DOVs in every $2' \times 2'$ grid) determined by altimeter data, the empirical formula as follows:

$$\begin{aligned} m_{\Delta\hat{g}} &= \sqrt{\beta_0^2 + \beta_1 \rho (C_{nn})^{-1}} \\ C_{nn} &= \frac{\beta_1 \rho}{m_{\Delta\hat{g}}{}^2 - \beta_0^2} \end{aligned} \tag{7}$$

where ρ is the density of the along-track DOVs, β_0 and β_1 are fitting parameter. Assuming that the NCEI ship-borne gravity anomaly, the altimeter-derived gravity anomaly and the global marine gravity anomaly model (SIO V30.1-GRA) are independent of each other, the STD of altimeter-derived gravity anomaly $m_{\Delta\hat{g}}$ can be obtained by the law of error propagation

$$\begin{bmatrix} \sigma_{BS}^2 \\ \sigma_{BN}^2 \\ \sigma_{SN}^2 \end{bmatrix} = \begin{bmatrix} 1\,1\,0 \\ 0\,1\,1 \\ 1\,0\,1 \end{bmatrix} \begin{bmatrix} \sigma_S^2 \\ \sigma_B^2 \\ \sigma_N^2 \end{bmatrix} \tag{8}$$

where σ_{BS}^2, σ_{BN}^2 and σ_{SN}^2 represent the covariance of the difference between altimeter-derived gravity anomalies and SIO V30.1-GRA model gravity anomalies, the covariance of the difference between altimeter-derived gravity anomalies and NCEI

TABLE II
RMS OF THE DIFFERENCE BETWEEN THE DIRECTIONAL COMPONENTS OF ALTIMETER-DETERMINED GRIDDED DOVS AND SIO V30.1-DOV MODEL IN DIFFERENT LSC CALCULATION WINDOWS UNIT: μRAD

Window/time(s)		0.1°/42	0.2°/271	0.3°/1648	0.4°/4169	0.5°/20717
HY-2A – SIO	meridian component	2.01	2.02	2.00	2.00	2.01
V30.1-DOV	prime vertical component	3.13	3.11	3.08	3.06	3.04
SARAL – SIO	meridian component	1.78	1.79	1.78	1.78	1.79
V30.1-DOV	prime vertical component	3.05	3.03	3.01	3.00	2.98
CryoSat-2 – SIO	meridian component	1.93	1.94	1.94	1.94	1.94
V30.1-DOV	prime vertical component	3.13	3.10	3.07	3.06	3.04

Time refers to CPU time (Intel(R) Core (TM) i7-4790 CPU @ 3.60 GHz).

ship-borne gravity anomalies, and the covariance of the difference between SIO V30.1-GRA model gravity anomalies and NCEI ship-borne gravity anomalies, respectively. σ_S^2, σ_B^2, and σ_N^2 represent the variance of SIO V30.1-GRA model gravity anomalies, altimeter-derived gravity anomalies and NCEI ship-borne gravity anomalies respectively.

B. Gravity Anomalies' Derivation

One-dimensional (1-D) FFT method and IVM formula are used to derive gravity anomalies from DOVs. Since the difference of latitude is taken into account in the calculation of spherical latitude by 1-D FFT method, the algorithm [46] is more rigorous in theory. In addition, compared with marine gravity anomalies directly derived from SSHs, the advantage of marine gravity anomalies derived from DOVs is that the DOVs are not affected by long wavelength error and crossover adjustment is not necessary in the calculation of DOVs. Therefore, IVM [51], [52] is used to derive the marine gravity anomalies

$$\Delta g(p) = \frac{\gamma_0}{4\pi} \int\int_{\sigma} H'(\psi)(\xi_q \cos\alpha_{qp} + \eta_q \sin\alpha_{qp}) d\sigma_q \quad (9)$$

where $\Delta g(p)$ is the gravity anomaly at point p, $\gamma_0 = \frac{GM}{R^2}$ (GM is the gravitational constant, R is the mean earth radius), α_{qp} is the azimuth from point q to point p; ξ_q and η_q are the meridian component and the prime vertical component of the DOV at point q respectively. $H'(\psi)$ is the derivative of kernel function

$$H'(\psi) = -\frac{\cos\frac{\psi}{2}}{2\sin^2\frac{\psi}{2}} + \frac{\cos\frac{\psi}{2}(3 + 2\sin\frac{\psi}{2})}{2\sin\frac{\psi}{2}(1 + \sin\frac{\psi}{2})} \quad (10)$$

where ψ is the spherical distance between p and q.

ψ cannot be zero in the derivative of kernel function $H'(\psi)$, so it is necessary to consider the influence of inner zone effect on gravity anomaly derivation

$$\Delta g = \frac{s_0\gamma_0}{2}(\xi_x + \eta_y) \quad (11)$$

$$s_0 = \sqrt{\frac{R^2\Delta\lambda\Delta\varphi\cos\varphi}{\pi}} \quad (12)$$

$$\xi_x(i) = \frac{1}{2R\Delta\varphi}\left[\xi(i+1) - \xi(i-1)\right] \quad (13)$$

$$\eta_y(i) = \frac{1}{2R\Delta\lambda\cos\varphi}\left[\eta(i+1) - \eta(i-1)\right] \quad (14)$$

where ξ_x and η_y are the change rates of the meridian and prime vertical component of the DOV, respectively; s_0 is the size of the inner zone. $\Delta\lambda$ and $\Delta\varphi$ are the difference of longitude and latitude, respectively.

IV. RESULTS AND ANALYSIS

A. DOVs' Calculation

The along-track DOVs and gridded DOVs are obtained with the above method. When LSC is used to estimate gridded DOVs, the different calculation window will cause the difference of the quantity and the distribution of the along-track geoid gradients, which affect the accuracy of DOVs. The influence of the size of the LSC calculation window on DOV precision should be considered when establishing high-precision gridded DOVs. Table II gives the RMS of the difference between altimeter-determined gridded DOVs and SIO V30.1-DOV model under different LSC calculation windows.

The Sentinel-3B-determined along-track DOVs and altimeter-determined DOVs are independent of each other. The influence of different LSC calculation window on gridded DOVs' precision is also assessed by Sentinel-3B altimetry data. First, altimeter-determined gridded DOVs are used to interpolate the meridian components and the prime vertical components at observation points of Sentinel-3B. Second, the along-track DOVs [4] determined by gridded DOVs at observation points of Sentinel-3B are calculated by

$$\varepsilon_{satellite} = \xi\cos\alpha + \eta\sin\alpha \quad (15)$$

where, ξ and η are the meridian components and the prime vertical components at observation points of Sentinel-3B, which are interpolated from altimeter-determined gridded DOVs; α is the along-track azimuth of Sentinel-3B.

Third, the along-track DOVs of Sentinel-3B are determined from the along-track geoid gradients which are calculated from Sentinel-3B-measured SSHs. Finally, the statistic information on differences between the along-track DOVs calculated from altimeter-determined DOVs and those calculated from Sentinel-3B-measured SSHs under different windows is given in Table III. The differences between satellite-determined and Sentinel-3B-calculted along-track DOVs are expressed as satellite—Sentinel-3B, e.g., HY-2A—Sentinel-3B, SARAL—Sentinel-3B, and CryoSat-2—Sentinel-3B.

As shown in Fig. 3, when the spherical distance is greater than 0.1°, the covariance of the longitudinal and the transverse component of DOV is close to 0. In order to achieve the optimal accuracy, the LSC window is selected at an interval of 0.1°. It

TABLE III
RMS OF THE DIFFERENCE OF THE ALONG-TRACK DOVS CALCULATED FROM THE ALTIMETRY DATA OF THREE SATELLITES AND SENTINEL-3B IN DIFFERENT CALCULATION WINDOWS OF LSC UNIT: μRAD

Window	0.1°	0.2°	0.3°	0.4°	0.5°
HY-2A – Sentinel-3B	4.38	4.38	4.39	4.37	4.37
SARAL – Sentinel-3B	4.30	4.30	4.29	4.29	4.29
CryoSat-2 – Sentinel-3B	4.35	4.35	4.34	4.34	4.34

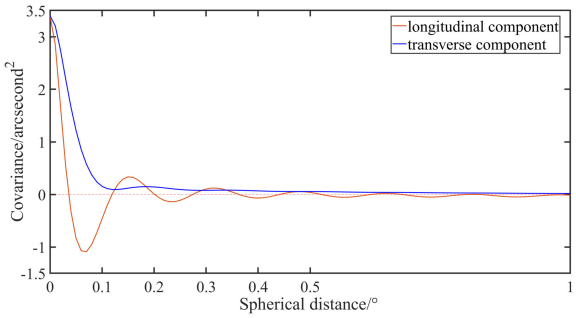

Fig. 3. Relationship between the covariance of the longitudinal and the transverse component of the DOVs and the spherical distance.

can be seen from Table II that the influence of LSC window size on the prime vertical component is greater than that of meridian component. With the increasing window size, the RMS of the difference of the prime vertical component calculated from three satellite altimetry data and SIO V30.1-DOV model is decreasing gradually, while the RMS of the difference of meridian component remains unchanged. This is because the orbit of altimeter is around 90°, and the along-track DOVs contain more signals in the meridional direction. Compared with prime vertical component, higher accuracy on the meridional component can be obtained from less altimeter data in a small calculation window. Table III gives that RMS of the along-track DOVs calculated from the altimeter-determined DOVs and Sentinel-3B-measured SSHs has a small change with the increase of window. With the increasement of the window, the time increases exponentially. Therefore, 0.4° can be the optimum window under comprehensive considering.

B. Accuracy Evaluation of DOVs Derivation

The 2′×2’ gridded DOVs are determined from three satellite altimetry data by LSC over the BOB and its adjoining area, and shown in Fig. 4.

The altimeter-determined along-track DOVs at observation points of Sentinel-3B are calculated from altimeter-determined DOVs and from Sentinel-3B-measured SSHs in the same way described in Section IV-A, respectively. After obtaining the STD of satellite—Sentinel-3B, the accuracy of the satellite-determined DOVs can be compared according to the law of error propagation (the accuracy of the Sentinel-3B-determined DOVs is constant). If the STD of satellite—Sentinel-3B is smaller, it indicates that the accuracy of altimeter-determined DOVs is higher. The statistical information is given in Table IV.

Table IV gives that the STD of HY-2A—Sentinel-3B is the maximum and that of SARAL—Sentinel-3B is the minimum,

TABLE IV
STATISTICAL RESULTS OF THE DIFFERENCE BETWEEN ALONG-TRACK DOVS CALCULATED FROM HY-2A, SARAL, CRYOSAT-2 AND SENTINEL-3B UNIT: μRAD

Data	Max	Min	Mean	STD	RMS
HY-2A – Sentinel-3B	62.75	-46.83	-0.04	4.37	4.37
SARAL – Sentinel-3B	61.89	-46.16	-0.05	4.29	4.29
CryoSat-2 – Sentinel-3B	61.66	-46.04	-0.05	4.34	4.34

but the difference between them is less than 0.1 μrad. Therefore, the accuracy of HY-2A-determined DOVs is similar to that of SARAL and CryoSat-2.

The data of pass0094 from cycle20 to cycle33 in Sentinel-3B of L2P are selected to calculate the along-track DOVs, and the along-track DOVs at observation points of Sentinel-3B are also calculated by altimeter-determined gridded DOVs. Fig. 5(a) shows the difference between them in the wavenumber domain.

Pujol *et al.* [53] concluded that the difference of SSHs in the wavelength range of 25 to 175 km mainly reflects the error of SSH model when using the measured SSHs to evaluate the accuracy of SSH model. Therefore, it can be considered that the signal in the wavelength range of 25 to 175 km of the along-track DOVs’ difference mainly comes from the error of gridded DOVs. The power spectral density (PSD) of the along-track DOVs’ difference between the three satellites and Sentinel-3B in the wavelength range of 25 km to 175 km is shown in Fig. 5(b). As shown in Fig. 5(b), the PSD of SARAL—Sentinel-3B is slightly smaller than that of HY-2A—Sentinel-3B and CryoSat-2—Sentinel-3B, and the PSD of HY-2A—Sentinel-3B is similar to that of CryoSat-2—Sentinel-3B. For more intuitive display, the PSD of SARAL—Sentinel-3B and CryoSat-2—Sentinel-3B are divided by HY-2A—Sentinel-3B, respectively. The ratio is shown in Fig. 6. It can be seen from Fig. 6 that most of the ratios between the PSD of HY-2A—Sentinel-3B and SARAL—Sentinel-3B are above 1, so the accuracy of SARAL-determined gridded DOVs is slightly higher. The ratios between the PSD of HY-2A—Sentinel-3B and CryoSat-2—Sentinel-3B fluctuate up and down in 1. In addition, the average ratio between the PSD of HY-2A—Sentinel-3B and CryoSat-2—Sentinel-3B is close to 0 after the ratios subtracting 1, and is smaller than the average ratio 0.028 when replacing the CryoSat-2’s PSD by SARAL’s PSD. Therefore, the accuracy of HY-2A-determined gridded DOVs is consistent with that of CryoSat-2-determined gridded DOVs, and slightly lower than that of SARAL-determined gridded DOVs.

From Fig. 4, it can be seen that differences between the gridded DOVs determined from three-satellite altimetry data are not obvious. Therefore, the XGM2019e-DOV model is adopted to evaluate the accuracy of the meridian component and the prime vertical component determined from three altimeters data. The statistical information of the differences between them is given in Table V.

As can be seen from Table V, differences of the altimeters-determined meridian component and prime vertical component and those of the XGM2019e-DOV model are similar. The difference for the prime vertical component is significantly

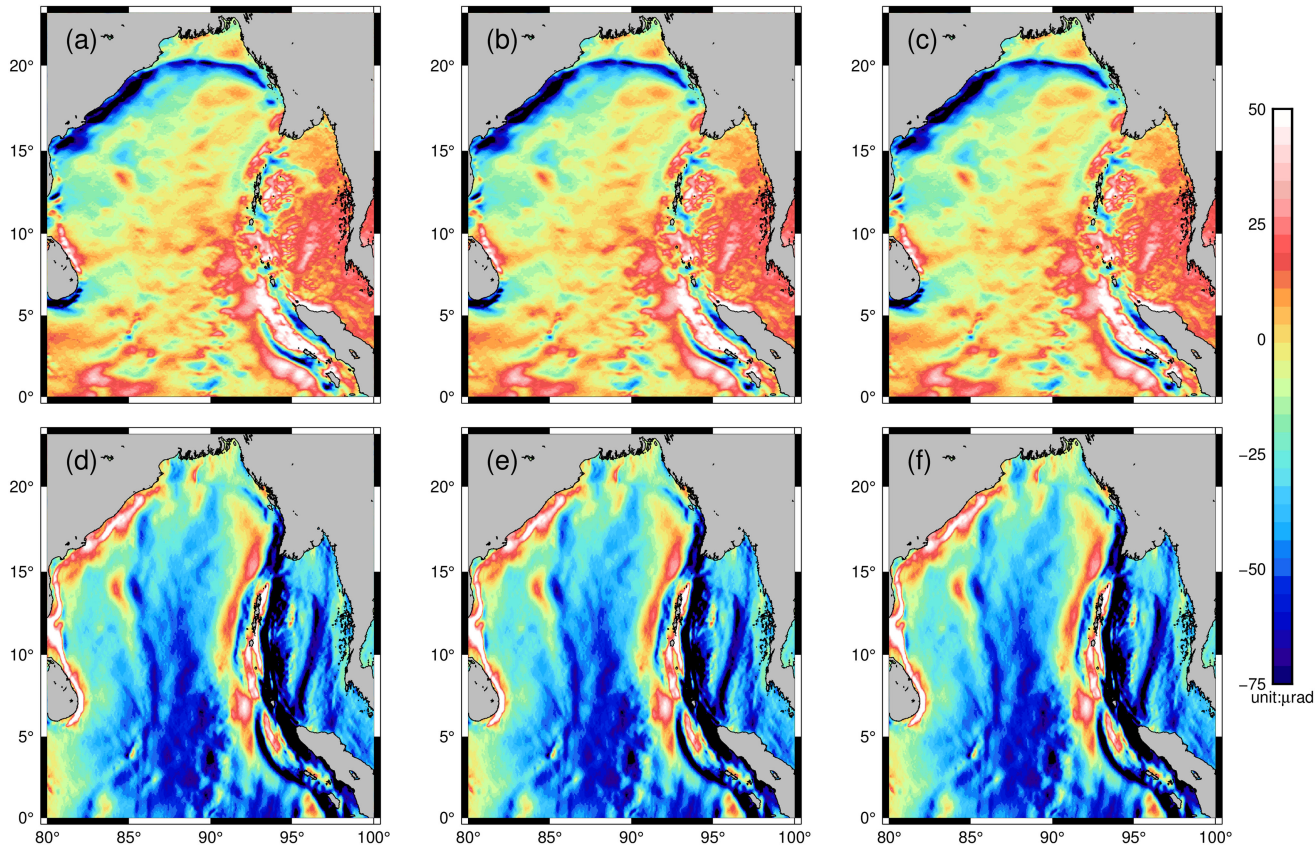

Fig. 4. DOVs determined from satellite altimetry data over the BOB. (a) and (d) Meridional component and the prime vertical component of the DOVs determined from HY-2A altimetry data, respectively. (b) and (e) Meridional component and the prime vertical component of the DOVs determined from SARAL altimetry data, respectively. (c) and (f) Meridional component and the prime vertical component of the DOVs determined from CryoSat-2 altimetry data, respectively.

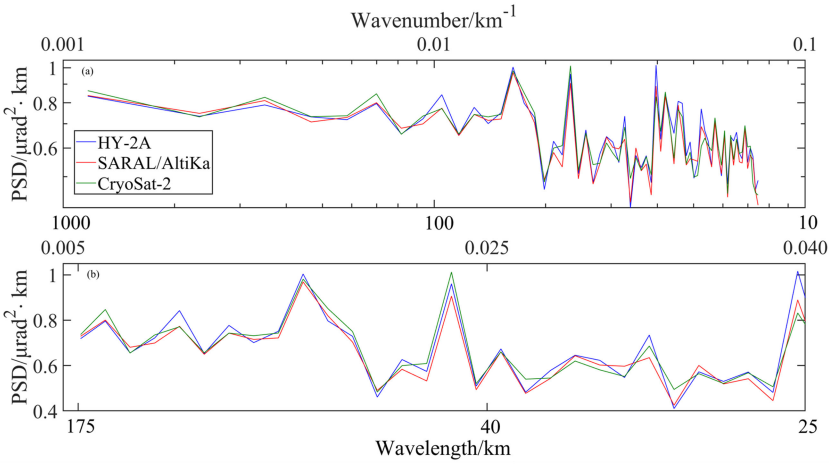

Fig. 5. Difference between the along-track DOVs of three altimeters and those of Sentinel-3B in wavenumber domain. (a) PSD of the difference of the along-track DOVs. (b) PSD of the difference of the along-track DOVs in the wavelength range of 25–175 km.

greater than that for the meridian component. This may be because the orbital inclination of altimeter is closer to the meridian direction, which makes the meridian component more accurate. The STD of difference between HY-2A-determined gridded DOVs and XGM2019e-DOV is consistent with that of difference between CryoSat-2-determined gridded DOVs and XGM2019e-DOV, and is slightly larger than that when replacing CryoSat-2 by SARAL. This is because SARAL works in the Ka band (35 GHz) and the frequency is higher than all previous altimeters.

Compared with the traditional Ku-band radar altimeter, such as HY-2A and CryoSat-2, SARAL has higher pulse repetition

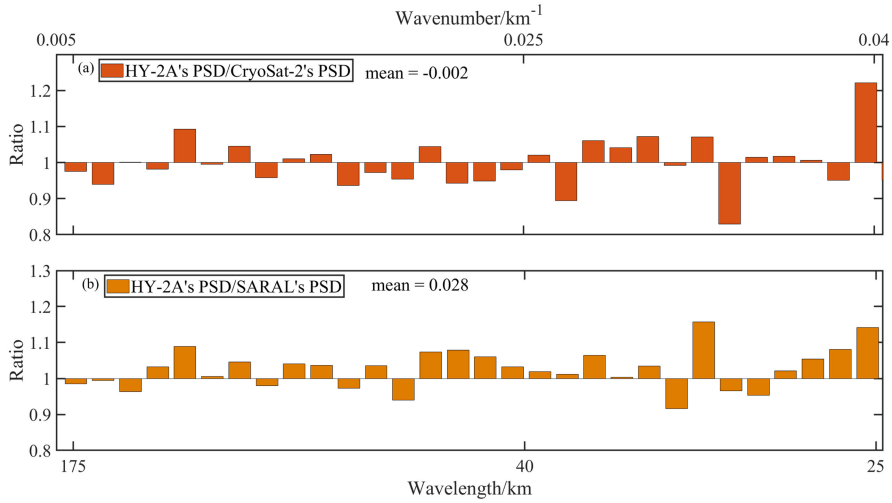

Fig. 6. Proportional relationship of PSD of the difference between along-track DOVs of three selected satellites and that of Sentinel-3B. (a) PSD ratios of data in (b) for HY-2A and CryoSat-2. (b) PSD ratios of data in (b) for HY-2A and SARAL.

TABLE V
STATISTICAL RESULTS OF THE DIFFERENCES OF THE MERIDIAN COMPONENT AND THE PRIME VERTICAL COMPONENT DETERMINED FROM THREE ALTIMETERS DATA (HY-2A, SARAL, AND CRYOSAT-2) AND XGM2019E-DOV UNIT: μRAD

Data	Directional components of DOVs	Max	Min	Mean	STD	RMS
HY-2A – XGM2019e-DOV	meridian component	24.43	-21.82	-0.09	1.87	1.87
	prime vertical component	25.61	-28.04	-0.03	2.14	2.14
SARAL – XGM2019e-DOV	meridian component	22.11	-22.43	-0.08	1.62	1.62
	prime vertical component	26.20	-28.01	-0.02	2.03	2.03
CryoSat-2 – XGM2019e-DOV	meridian component	22.90	-23.12	-0.10	1.87	1.87
	prime vertical component	27.73	-29.43	-0.02	2.16	2.16

frequency, which improves the precision of altimeter ranging and significant wave height. Therefore, the meridian component and the prime vertical component of SARAL-determined DOVs have higher accuracy. Besides, it is proposed in many studies that CryoSat-2 plays an important role in gravity anomalies derivation [31], [46], so CryoSat-2-determined DOVs have high accuracy. Therefore, it is feasible and reliable to use HY-2A altimetry data to derive DOVs.

From the diagrams of difference between HY-2A-determined, SARAL-determined, and CryoSat-2-determined gridded DOVs (see Fig. 7), it can be seen that the average difference of meridian components between HY-2A-determined DOVs and SARAL-determined DOVs is less than that when replacing SARAL DOVs by CryoSat-2. The average difference of prime vertical components between HY-2A-determined DOVs and SARAL-determined DOVs is consistent with that of prime vertical components between HY-2A-determined DOVs and CryoSat-2-determined DOVs. The STD of the difference of meridian components and prime vertical components between HY-2A-determined and SARAL-determined gridded DOVs is smaller than that of difference between HY-2A-determined and CryoSat-2-determined gridded DOVs. In general, the accuracy of HY-2A-determined gridded DOVs is consistent with that of CryoSat-2, and is slightly lower than that of SARAL.

TABLE VI
RESULTS OF THE FITTING PARAMETERS β_0 AND β_1

	$m_{\Delta g}$ /mGal	C_{nn} /″	$(\beta_0)^2$	β_1
HY-2A	2.75	1.80	8.36	-7.95
CryoSat-2	2.59	2.05		

C. Accuracy Evaluation of Gravity Anomalies Derivation

IVM is applied to determine the $2' \times 2'$ gravity anomalies over the BOB and its adjoining area from altimeter-derived gridded DOVs, and the gravity anomalies are shown in Fig. 8.

XGM2019e-GRA, SIO V30.1-GRA model gravity anomalies and NCEI ship-borne gravity anomalies are used to evaluate the accuracy of gravity anomalies derived from altimetry data of three satellites. The statistical results of the differences between the altimeter-derived gravity anomalies and XGM2019e-GRA, SIO V30.1-GRA, ship-borne gravity anomalies are given in Table VII.

In the process of deriving gravity anomalies, the noise variance of the along-track DOVs for SARAL need to be calculated by iteration: the initial noise variance matrix of SARAL is calculated based on (5); gravity anomalies are derived by IVM based on SARAL-determined gridded DOVs and the STD of gravity anomaly is calculated by (8); the STD of gravity anomaly

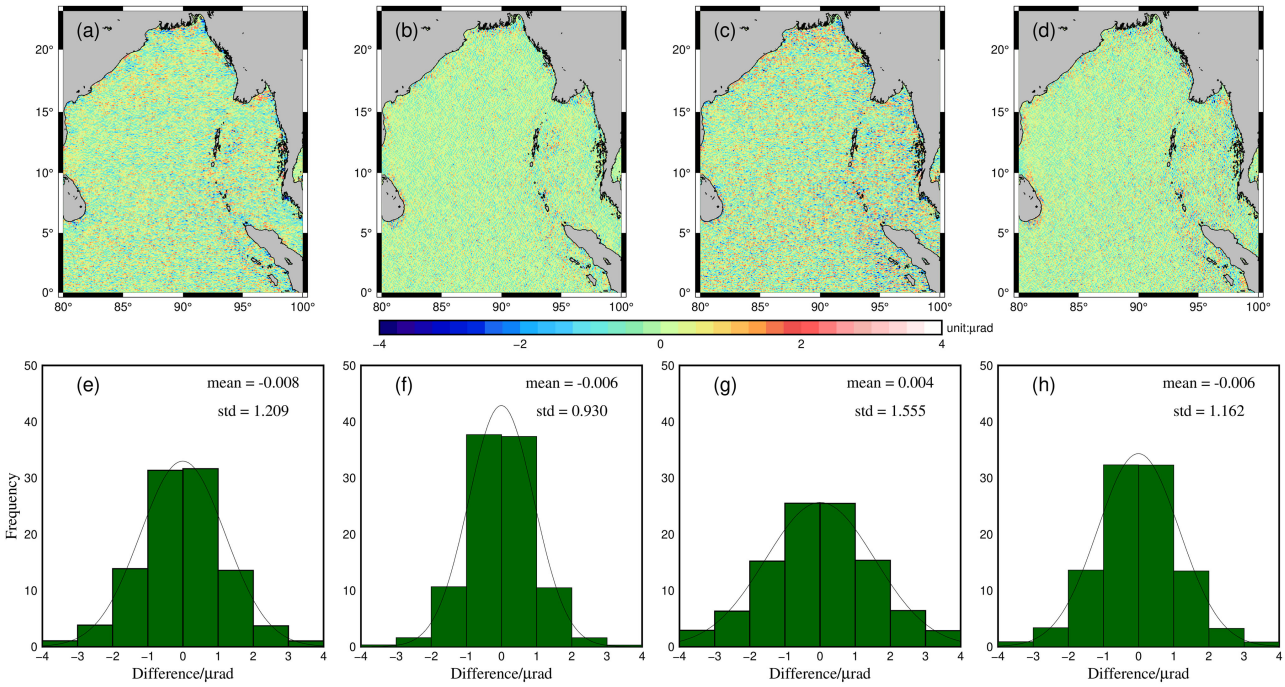

Fig. 7. Difference between the gridded HY-2A-determined DOVs and SARAL-determined DOVs, CryoSat-2-determined DOVs. (a), (b), (e), and (f) Difference distribution of meridian component and prime vertical component of gridded HY-2A-determined DOVs and SARAL-determined DOVs, and the distribution in each interval respectively. (c), (d), (g), and (h) Difference distribution of meridian component and prime vertical component of gridded HY-2A-determined DOVs and CryoSat-2-determined DOVs, and the distribution in each interval respectively.

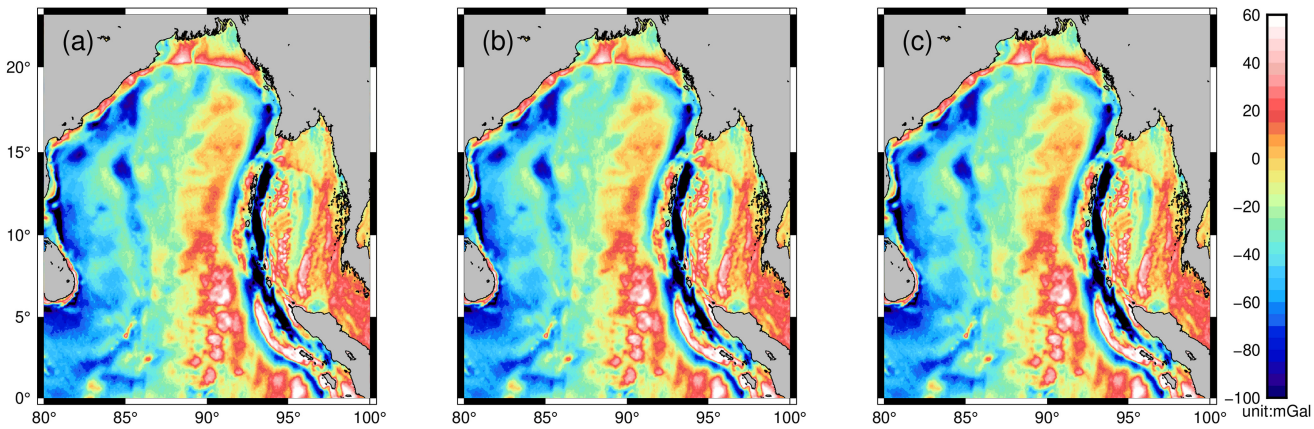

Fig. 8. Gravity anomalies over the BOB and its adjoining area. (a)–(c) Gravity anomalies determined by HY-2A-derived DOVs, SARAL-derived DOVs and CryoSat-2-derived DOVs, respectively.

is substituted into the empirical formula to obtain a new noise variance matrix, and the new STD of gravity anomaly is obtained according to the above steps; repeat the above steps until the difference of two adjacent STD of SARAL-derived gravity anomalies is less than 0.02 mGal. β_0 and β_1 in (7) are calculated according to the noise variances of altimeter-determined DOVs and the precision of altimeter-derived gravity anomalies (from HY-2A and CryoSat-2). The calculation results are given in Table VI.

The difference between meridian component of gridded SARAL-determined DOVs and SIO V30.1 is reduced by 0.01 μrad, and the difference of prime vertical component is reduced by 0.07 μrad after the accuracy of the along-track DOVs evaluated by empirical formula and iterative method. The accuracy of SARAL-derived gravity anomalies is also improved by 0.10 mGal. The above results show that it is suitable to evaluate the accuracy of Ka-band along-track DOVs by the iteration method.

The similar gravity anomalies derived from three satellite altimetry data is shown in Fig. 9. As can be seen from Table VII, the mean of difference between altimeter-derived and NCEI ship-borne gravity anomalies tends to 0 mGal and is less than

TABLE VII
STATISTICAL RESULTS OF THE DIFFERENCES BETWEEN THE ALTIMETER-DERIVED GRAVITY ANOMALIES AND SIO V30.1-GRA, XGM2019E-GRA MODEL GRAVITY ANOMALIES, NCEI SHIP-BORNE GRAVITY ANOMALIES UNIT: MGAL

Data	Max	Min	Mean	STD	RMS
HY-2A – NCEI	32.00	-31.44	-0.08	4.91	4.91
HY-2A – SIO V30.1-GRA	103.26	-97.88	0.36	3.64	3.66
HY-2A – XGM2019e-GRA	36.07	-36.58	-0.14	2.70	2.70
SARAL – NCEI	31.57	-30.01	-0.09	4.86	4.86
SARAL – SIO V30.1-GRA	100.76	-96.75	0.36	3.53	3.55
SARAL – XGM2019e-GRA	34.47	-35.13	-0.14	2.55	2.55
CryoSat-2 – NCEI	34.15	-30.51	-0.06	4.92	4.92
CryoSat-2 – SIO V30.1-GRA	99.74	-96.29	0.36	3.59	3.61
CryoSat-2 – XGM2019e-GRA	36.55	-34.42	-0.14	2.70	2.70
SIO V30.1-GRA – NCEI	42.70	-33.22	-0.70	4.78	4.83
XGM2019e-GRA – NCEI	29.95	-30.09	-0.13	5.09	5.10

TABLE VIII
ACCURACY OF ALTIMETER-DERIVED GRAVITY ANOMALIES AT DIFFERENT DISTANCES AWAY FROM COASTLINE UNIT: MGAL

Data	Distance away from the coastline/km	Number	Max	Min	Mean	STD	RMS
HY-2A – NCEI	<12	312	20.24	-21.45	-1.07	7.84	7.91
	12-24	1782	29.83	-24.92	0.34	6.61	6.62
	24-36	3603	24.13	-25.53	0.15	5.60	5.60
	36-48	3479	19.53	-30.05	0.30	4.80	4.81
	>48	44363	32.00	-31.44	-0.14	4.75	4.75
SARAL – NCEI	<12	312	19.52	-21.27	-0.66	7.74	7.77
	12-24	1782	27.53	-24.91	0.27	6.45	6.46
	24-36	3603	23.96	-24.70	0.02	5.53	5.53
	36-48	3479	20.21	-28.73	0.34	4.83	4.85
	>48	44363	31.57	-30.01	-0.14	4.70	4.70
CryoSat-2 – NCEI	<12	312	19.28	-22.65	-0.34	7.53	7.54
	12-24	1782	30.23	-25.80	0.64	6.61	6.64
	24-36	3603	24.08	-23.41	0.30	5.56	5.57
	36-48	3479	20.72	-28.94	0.25	4.95	4.95
	>48	44363	34.15	-30.51	-0.14	4.75	4.75
SIO V30.1 - NCEI	<12	312	32.35	-22.95	-1.77	7.72	7.92
	12-24	1782	32.62	-23.41	-0.83	6.24	6.30
	24-36	3603	31.00	-22.95	-1.10	5.44	5.55
	36-48	3479	18.60	-25.45	-0.69	4.65	4.70
	>48	44363	42.70	-33.22	-0.66	4.56	4.61

that between SIO V30.1 model and NCEI ship-borne gravity anomalies. Because EGM2008 model is applied to calibrate the long wave of ship-borne gravity data and used as the reference gravity field model in the remove-restore procedure. However, the accuracy of altimeter-derived gravity anomalies is lower than that of SIO V30.1 because SIO V30.1 integrates altimetry data from multiple satellites, and the amount of data is much larger than that of a single satellite. In addition, the RMS of difference between HY-2A-derived gravity anomalies and NCEI ship-borne gravity anomalies is similar to that of difference determined by SARAL and CryoSat-2. The results are also the same characteristic when changing NCEI ship-borne

gravity anomalies into model gravity anomalies, such as SIO V30.1-GRA and XGM2019e-GRA. Therefore, the accuracy of gravity anomalies derived from HY-2A altimeter data is similar to that of gravity anomalies derived from SARAL altimeter data and gravity anomalies derived from CryoSat-2 altimeter data.

The echo waveform of satellite altimeter is easy to be polluted in the nearshore, and the maximum estimation error of ocean tidal model in the nearshore is much larger than that in the open ocean. Therefore, the connection between the accuracy of gravity anomalies and the distance away from the coastline is also discussed. Table VIII gives the accuracy of gravity anomalies derived by altimeter-determined DOVs at different distances away from the coastline. Obviously, the accuracy of gravity anomalies increases with the increasing distance away from the coastline. The RMS of differences between HY-2A-derived gravity anomalies and NCEI ship-borne gravity anomalies is the largest at 0–12 km away from the coastline. However, when the distance away from the coastline is more than 48 km, the RMS of differences between HY-2A-derived and NCEI ship-borne gravity anomalies is consistent with that of the difference between CryoSat-2-derived and NCEI ship-borne gravity anomalies. Thus, compared with the CryoSat-2-derived and SARAL-derived gravity anomalies, the accuracy of HY-2A-derived gravity anomalies is more affected by the coastline, but with the increase of the distance away from the coastline, the accuracy of HY-2A-derived gravity anomalies is significantly improved. In addition, the accuracy of single-altimeter-derived gravity anomalies is less than that of SIO V30.1 model which uses waveform retracked altimetry data. The above results show that land or island will have an impact on the gravity anomalies recovery. Reprocessing the data near the coastline is very important to obtain high-precision gravity anomalies.

The process of calculating altimeter-determined DOVs can effectively weaken the influence of low-frequency errors, such as radial orbit error. The DOVs also reflect high-frequency information of marine gravity field, so DOVs are widely used in the construction of gravity anomaly model. The accuracy of DOVs is closely related to the accuracy of gravity anomalies derivation. Therefore, by comparing the accuracy of altimeter-derived gravity anomalies derivation, it is also verified that the accuracy of HY-2A-determined DOVs is similar to that of CryoSat-2-determined DOVs, and slightly lower than that of SARAL-determined DOVs.

V. Conclusion

HY-2A is the first marine dynamic environment satellite launched by China. It was successfully launched in August 2011 and stopped collecting data in Sept. 2020. The main purpose of this article is to evaluate the accuracy of HY-2A/GM-determined DOVs in the BOB. The accuracy of HY-2A/GM-determined DOVs is evaluated by comparing with the accuracy of SARAL/AltiKa-determined and CryoSat-2-determined DOVs in the same period. First, the along-track DOVs calculated from the SSHs of Sentinel-3B L2P product (from cycle 20 to cycle 33) are used to evaluate the accuracy of altimeter-determined gridded DOVs. Then, Sentinel-3B-measured SSHs of pass 0094 from cycle 20 to cycle 33 are used to analyze the accuracy of the DOVs determined by the altimeters'data in the wavenumber domain, and the accuracy of $2' \times 2'$ altimeter-determined gridded DOVs is assessed by XGM2019e-DOV model. Gravity anomaly models determined by altimeter-determined gridded DOVs are established. The accuracy of altimeter-determined gridded DOVs can also be assessed through the accuracy of gravity anomalies derivation. The results are as follows.

Compared with the along-track DOVs calculated from Sentinel-3B measured SSHs, the STD of the difference for the along-track DOVs from HY-2A-derived DOVs is 0.03 and 0.08 μrad greater that for CryoSat-2 and SARAL, respectively. The mean of PSD ratios of differences between along-track DOVs calculated from Sentinel-3B-measured SSHs and obtained from HY-2A-determined gridded DOVs is similar to that when replacing HY-2A by CryoSat-2, and greater than that when replacing HY-2A by SARAL. In addition, the STD of the difference between HY-2A-determined DOVs and XGM2019e-DOV is consistent with that of the difference between CryoSat-2-determined DOVs and XGM2019e-DOV. Therefore, the accuracy of DOVs calculated from HY-2A-measured is similar to that of CryoSat-2-measured SSHs, and lower than that of SARAL-determined DOVs.

The RMS of differences between HY-2A-derived and NCEI ship-borne gravity anomalies is consistent with that when replacing HY-2A by CryoSat-2 and is slightly higher than that when replacing HY-2A by SARAL. Therefore, the accuracy of HY-2A-derived gravity anomalies is similar to that of CryoSat-2-derived gravity anomalies, and slightly lower than that of SARAL-derived gravity anomalies. Moreover, with the increase of the distance away from the coastline, the accuracy of HY-2A-derived gravity anomalies is significantly improved. Therefore, from the performance of HY-2A/GM-derived gravity anomalies, it can be verified that the accuracy of HY-2A/GM-derived DOVs is high.

In conclusion, the performance of HY-2A/GM altimetry data is similar to that of CryoSat-2 and SARAL, and the HY-2A/GM data can be adopted to determine high-precision DOV models.

References

[1] J. Guo, J. Qin, Q. Kong, and G. Li, "On simulation of precise orbit determination of HY-2 with centimeter precision based on satellite-borne GPS technique," *Appl. Geophys.*, vol. 9, no. 1, pp. 95–107, Mar. 2012.

[2] C. Hwang, T. P. Tseng, T. J. Lin, D. Švehla, U. Hugentobler, and B. F. Chao, "Quality assessment of FORMOSAT-3/COSMIC and GRACE GPS observables: Analysis of multipath, ionospheric delay and phase residual in orbit determination," *GPS Solution*, vol. 14, no. 1, pp. 121–131, Jan. 2010.

[3] J. Guo, Y. Wang, Y. Shen, X. Liu, Y. Sun, and Q. Kong, "Estimation of SLR station coordinates by means of SLR measurements to kinematic orbit of LEO satellites," *Earth Planets Space*, vol. 70, no. 1, Dec. 2018, Art. no. 201.

[4] C. Hwang and R. Kao, "TOPEX/POSEIDON-derived space-time variations of the Kuroshio current: Applications of a gravimetric geoid and wavelet analysis," *Geophys. J. Int.*, vol. 151, no. 3, pp. 835–847, Dec. 2002.

[5] K. S. Krishna *et al.*, "Tectonics of the ninety east ridge derived from spreading records in adjacent oceanic basins and age constraints of the ridge," *J. Geophys. Res. Solid Earth*, vol. 117, no. B4, Dec. 2012.

[6] M. H. Rio, S. Mulet, and N. Picot, "Beyond GOCE for the ocean circulation estimate: Synergetic use of altimetry, gravimetry, and in situ data provides new insight into geostrophic and Ekman currents," *Geophys. Res. Lett.*, vol. 41, no. 24, pp. 8918–8925, Dec. 2014.

[7] B. Tozer, D. T. Sandwell, W. H. F. Smith, C. Olson, J. R. Beale, and P. Wessel, "Global bathymetry and topography at 15 arc sec: SRTM15+," *Earth Space Sci.*, vol. 6, no. 10, pp. 1847–1864, Oct. 2019.

[8] J. A. Griggs and J. L. Bamber, "Antarctic ice-shelf thickness from satellite radar altimetry," *J. Glaciol.*, vol. 57, no. 203, pp. 485–498, Jun. 2011.

[9] A. A. Ardalan and H. Hashemi, "Empirical global ocean tide Mean Sea Level modeling using satellite altimetry data case study: A new empirical global ocean tide and mean Sea Level model based on Jason-1 satellite altimetry observations," *Lecture Notes Earth Sci.*, vol. 112, pp. 175–221, Jan. 2008.

[10] X. Wan, R. F. Annan, S. Jin, and X. Gong, "Vertical deflections and gravity disturbances derived from HY-2A data," *Remote Sens.*, vol. 12, no. 14, Jul. 2020.

[11] Q. Y. Li and L. Sun, "Technical note: Watershed strategy for oceanic mesoscale eddy splitting," *Ocean Sci.*, vol. 11, no. 2, pp. 269–273, May 2015.

[12] J. Guo, Y. Shen, K. Zhang, X. Liu, Q. Kong, and F. Xie, "Temporal-spatial distribution of oceanic vertical deflections determined by TOPEX/Poseidon and Jason-1/2 missions," *Earth Sci. Res. J.*, vol. 20, no. 2, pp. H1–H5, Dec. 2016.

[13] C. Jekeli, "An analysis of vertical deflections derived from high-degree spherical harmonic models," *J. Geodesy*, vol. 73, no. 1, pp. 10–22, Feb. 1999.

[14] I. N. Tziavos and V. D. Andritsanos, "Improvements in the computation of deflections of the vertical by FFT," *Phys. Chem. Earth*, vol. 23, no. 1, pp. 71–75, Dec. 1998.

[15] H. Wang, Y. Wang, H. Chai, and L. Bao, "$1' \times 1'$ Vertical deflection and its precision evaluation on China west Pacific Ocean region," *Acta Geodaetica et CartographicaSinica*, vol. 46, no. 9, pp. 1073–1079, Sep. 2017.

[16] X. Wan, R. Zhang, Y. Li, B. Liu, and X. Sui, "Matching relationship between precisions of gravity anomaly and vertical deflections in terms of spherical harmonic function," *Acta Geodaetica et CartographicaSinica*, vol. 46, no. 6, pp. 706–713, Jun. 2017.

[17] D. T. Sandwell, "Antarctic marine gravity field from high-density satellite altimetry," *Geophys. J. Int.*, vol. 109, no. 2, pp. 437–448, Jun. 1992.

[18] A. Olgiati, G. Balmino, M. Sarrailh, and C. M. Green, "Gravity anomalies from satellite altimetry: Comparison between computation via geoid heights and via deflections of vertical," *J. Geodesy.*, vol. 69, no. 4, pp. 252–260, Dec. 1995.

[19] C. Hwang, "Inverse vening meinesz formula and deflection-geoid formula: Applications to the predictions of gravity and geoid over the South China Sea," *J. Geodesy.*, vol. 72, no. 5, pp. 304–312, May 1998.

[20] M. Jiang, K. Xu, and Y. Liu, "Calibration and validation of reprocessed HY-2A altimeter wave height measurements using data from Buoys, Jason-2, cryosat-2 and SARAL/AltiKa," *J. Atmos. Ocean Tech.*, vol. 35, no. 6, pp. 1331–1352, Apr. 2018.

[21] Q. Liu, K. Xu, M. Jiang, and J. Wang, "Preliminary marine gravity field from HY-2A/GM altimeter data," *Acta Oceanol. Sinica*, vol. 39, no. 7, pp. 127–134, Aug. 2020.

[22] L. Bao *et al.*, "First accuracy assessment of the HY-2A altimeter sea surface height observations: Cross-calibration results," *Adv. Space Res.*, vol. 55, no. 1, pp. 90–105, Jan. 2015.

[23] S. Zhang, J. Li, T. Jin, and D. Che, "HY-2A altimeter data initial assessment and corresponding two-pass waveform retracker," *Remote Sens.*, vol. 10, no. 4, Mar. 2018, Art. no. 507.

[24] C. Zhu, J. Guo, C. Hwang, J. Gao, J. Yuan, and X. Liu, "How HY-2A/GM altimeter performs in marine gravity derivation: Assessment in the South China Sea," *Geophys. J. Int.*, vol. 219, no. 2, pp. 1056–1064, Nov. 2019.

[25] M. Radhakrishna, G. S. Rao, N. Satyabrata, B. Rastic, and D. Twinkle, "Early cretaceous fracture zones in the Bay of Bengal and their tectonic implications: Constraints from multi-channel seismic reflection and potential field data," *Tectonophysics*, vol. 522/523, pp. 187–197, Feb. 2012.

[26] M. Alam, M. M. Alam, J. R. Curray, M. L. R. Chowdhury, and M. R. Gani, "An overview of the sedimentary geology of the Bengal Basin in relation to the regional tectonic framework and basin-fill history," *Sedimentary Geol.*, vol. 155, no. 3/4, pp. 179–208, Feb. 2003.

[27] *Along-Track Level-2+ (L2P) SLA Product Handbook*, 2nd ed., USA, 2020.

[28] H. Zhang, Q. Wu, and G. Chen, "Validation of HY-2A Remotely Sensed Wave Heights against Buoy Data and Jason-2 Altimeter Measurements," *J. Atmos. Ocean Tech.*, vol. 32, no. 6, pp. 1270–1280, Jun. 2015.

[29] C. Zhu, X. Liu, J. Guo, S. Yu, and Y. Gao, "Sea surface heights and marine gravity determined from SARAL/AltiKa Ka-band altimeter over South China Sea," *Pure Appl. Geophys.*, vol. 178, no. 1, pp. 1513–1527, Apr. 2021.

[30] H. S. Hector, Q. Pierre, and A. Fabrice, "Assessment of SARAL/AltiKa wave height measurements relative to Buoy, Jason-2, and Cryosat-2 data," *Mar. Geodesy*, vol. 38, no. 1, pp. 449–465, Sep. 2015.

[31] D. T. Sandwell, R. D. Mueller, W. H. F. Smith, E. Garcia, and R. Francis, "New global marine gravity model from cryosat-2 and jason-1 reveals buried tectonic structure," *Science*, vol. 346, no. 6205, pp. 65–67, Oct. 2014.

[32] L. Stenseng and O. B. Andersen, "Preliminary gravity recovery from Cryosat-2 data in the Baffin Bay," *Adv. Space Res.*, vol. 50, no. 8, pp. 1158–1163, Oct. 2012.

[33] S. Labroue, F. Boy, N. Picot, M. Urvoy, and M. Ablain, "First quality assessment of the Cryosat-2 altimetric system over ocean," *Adv. Space Res.*, vol. 50, no. 8, pp. 1030–1045, Oct. 2012.

[34] *CryoSat Mission and Data Description*, 3rd ed., European, 2007.

[35] G. Dibarboure and M. I. Pujol, "Improving the quality of Sentinel-3A data with a hybrid mean sea surface model, and implications for Sentinel-3B and SWOT," *Adv. Space Res.*, vol. 68, no. 2, pp. 1116–1139, Jul. 2021.

[36] D. T. Sandwell, H. Harper, B. Tozer, and W. H. F. Smith, "Gravity field recovery from geodetic altimeter missions," *Adv. Space Res.*, vol. 68, pp. 1059–1072, Sep. 2019.

[37] P. Zingerle, R. Pail, T. Gruber, and X. Oikonomidou, "The combined global gravity field model XGM2019e," *J. Geodesy*, vol. 94, no. 7, Jul. 2020, Art. no. 66.

[38] J. Guo, X. Liu, Y. Chen, J. Wang, and C. Li, "Local normal height connection across sea with ship-borne gravimetry and GNSS techniques," *Mar. Geophys. Res.*, vol. 35, no. 2, pp. 141–148, Jan. 2014.

[39] P. Wessel and T. M. Chandler, "The mgd77 supplement to the generic mapping tools," *Comput. Geosci.*, vol. 33, no. 1, pp. 62–75, May 2007.

[40] F. S. Paolo and E. C. Molina, "Integrated marine gravity field in the brazilian coast from altimeter-derived sea surface gradient and shipborne gravity," *J. Geodyn.*, vol. 50, no. 5, pp. 347–354, Dec. 2010.

[41] R. H. Rapp, "Geos 3 data processing for the recovery of geoid undulations and gravity anomalies," *J. Geophys. Res. Atmos.*, vol. 84, no. B8, pp. 3784–3792, Aug. 1979.

[42] P. Knudsen, "Simultaneous estimation of the gravity field and sea surface topography from satellite altimeter data by least-squares collocation," *Geophys. J. Int.*, vol. 104, no. 2, pp. 307–317, Apr. 2007.

[43] R. Rummel, K. P. Schwarz, and M. Gerstl, "Least squares collocation and regularization," *J. Geodesy*, vol. 53, no. 4, pp. 343–361, Dec. 1979.

[44] S. Mulet *et al.*, "The new CNES-CLS18 global mean dynamic topography," *Ocean Sci.,* vol. 17, pp. 789–808, 2021.

[45] N. K. Pavlis, S. A. Holmes, S. C. Kenyon, and J. K. Factor, "The development and evaluation of the earth gravitational model 2008 (EGM2008)," *J. Geophys. Res. Solid Earth*, vol. 118, May 2013, Art. no. B04406.

[46] C. Hwang, E.-C. Kao, and B. Parsons, "Global derivation of marine gravity anomalies from Seasat, Geosat, ERS-1 and TOPEX/POSEIDON altimeter data," *Geophys. J. Int.*, vol. 134, no. 2, pp. 449–459, Aug. 1998.

[47] H. Moritz, *Advanced Physical Geodesy*. Karlsruhe, Germany: Herbert Wichmann, 1980.

[48] C. Hwang and B. Parsons, "Gravity anomalies derived from seasat, geosat, ERS-I and TOPEX/POSEIDON altimetry and ship gravity: A case study over the Reykjanes ridge," *Geophys. J. Int.*, vol. 122, no. 2, pp. 551–568, Sep. 1995.

[49] C. C. Tscherning and R. H. Rapp, "Closed covariance expressions for gravity anomalies, geoid undulations, and deflections of the vertical implied by anomaly degree variance models," Apr. 1974.

[50] H. Moritz, "Advanced least-squares methods," Jun. 1972.

[51] C. Zhu *et al.*, "Marine gravity determined from multi-satellite GM/ERM altimeter data over the South China Sea: SCSGA V1.0," *J. Geodesy*, vol. 94, May 2020, Art. no. 50.

[52] W. Liang, J. Li, X. Xu, S. Zhang, and Y. Zhao, "A high-resolution earth's gravity field model SGG-UGM-2 from GOCE, GRACE, satellite altimetry, and EGM2008," *Engineering*, vol. 6, no. 8, pp. 860–878, Aug. 2020.

[53] M. Pujol, P. Schaeffer, Y. Fauge're, M. Raynal, G. Dibarboure, and N. Picot, "Gauging the improvement of recent mean sea surface models: A new approach for identifying and quantifying their errors," *J. Geophys. Res. Oceans*, vol. 123, no. 8, pp. 5889–5911, Aug. 2018.

Hui Ji is currently working toward the M.S. degree in geodesy and surveying engineering with Shandong University of Science and Technology, Qingdao, China.

Her research interest includes marine gravity field derivation.

Jinyun Guo received the Ph.D. degree in geodesy and surveying engineering from Shandong University of Science and Technology, Qingdao, China, in 2004.

He is currently a Professor with the College of Geodesy and Geomatics, Shandong University of Science and Technology. His research interest includes space geodesy.

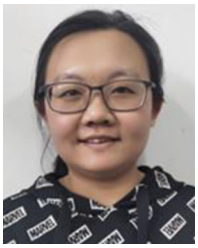

Chengcheng Zhu is currently working toward the Ph.D. degree in geodesy and surveying engineering with the Shandong University of Science and Technology, Qingdao, China.

Her current research interests include satellite altimetry and gravity data processing applications.

Jiajia Yuan is currently working toward the Ph.D. degree in geodesy and surveying engineering with Shandong University of Science and Technology, Qingdao, China.

His research interest includes multisatellite altimetry data processing and application.

Xin Liu received the Ph.D. degree in geodesy and surveying engineering from Shandong University of Science and Technology, Qingdao, China, in 2007.

She is currently an Associate Professor with the College of Geodesy and Geomatics, Shandong University of Science and Technology. Her research interests include spatial data processing and data mining.

Guowei Li received the M.S. degree in geodesy and surveying engineering from the Shandong University of Science and Technology, Qingdao, China, in 2013.

He is currently with Shandong Provincial Institute of Land Surveying and Mapping, Qingdao, China. His current research interest includes GNSS data processing and applications.